PLANETARY SCIENCE

Ferric iron stabilization at deep magma ocean conditions

Hongluo L. Zhang[1]*, Marc M. Hirschmann[2], Oliver T. Lord[3], Anja Rosenthal[4,5], Sergey Yaroslavtsev[4], Elizabeth Cottrell[6], Alexandr I. Chumakov[4], Michael J. Walter[7]

Fe_2O_3 produced in a deep magma ocean in equilibrium with core-destined alloy sets the early redox budget and atmospheric composition of terrestrial planets. Previous experiments (≲28 gigapascals) and first-principles calculations indicate that a deep terrestrial magma ocean produces appreciable Fe^{3+} but predict $Fe^{3+}/\Sigma Fe$ ratios that conflict by an order of magnitude. We present $Fe^{3+}/\Sigma Fe$ of glasses quenched from melts equilibrated with Fe alloy at 38 to 71 gigapascals, 3600 to 4400 kelvin, analyzed by synchrotron Mössbauer spectroscopy. These indicate $Fe^{3+}/\Sigma Fe$ of 0.056 to 0.112 in a terrestrial magma ocean with mean alloy-silicate equilibration pressures of 28 to 53 gigapascals, producing sufficient Fe_2O_3 to account for the modern bulk silicate Earth redox budget and surficial conditions near or more oxidizing than the iron-wüstite buffer, which would stabilize a primitive CO- and H_2O-rich atmosphere.

INTRODUCTION

A notable feature of Earth's accessible upper mantle is that it is comparatively oxidized relative to the metal-bearing primitive materials from which it accreted (*1*–*3*). The oxidation state of Earth's mantle affects its chemical and physical properties, including its rheology (*4*), melting behavior (*5*), and the abundance and speciation of volatiles (*6*). For example, the dominant terrestrial volcanic gases are H_2O and CO_2, rather than H_2 and CO, because the oxygen fugacity (fO_2) of Earth's upper mantle is nearly six orders of magnitude greater than would be expected for peridotitic silicate in equilibrium with Fe-rich alloy at low pressure (*5*, *7*).

Recently, attention has focused on the hypothesis that the oxidized character of Earth's mantle derived largely from the disproportionation of FeO to Fe_2O_3 and Fe in a deep magma ocean (*8*–*13*). Experiments and theoretical calculations show that silicate liquids in equilibrium with Fe-rich alloy have appreciable Fe_2O_3 at high pressures (*11*–*13*). These results imply that early atmospheres developed above magma oceans may be oxidized, with abundant H_2O and CO_2 (*6*, *8*, *11*, *12*, *14*, *15*), and indicate that the oxidation states of the interiors of rocky planets and exoplanets are directly related to their mass, which has notable implications for the relationship between the size of planets and their habitability (*16*).

Characteristic pressures of terrestrial core formation are thought to be between 28 and 53 GPa, which is established based on siderophile element partitioning of metal-silicate equilibration [see compilation in (*10*)], and even higher pressures are expected for super-earth exoplanets (*17*). But to date, there have been no experiments documenting the Fe_2O_3 content of molten silicate in equilibrium with alloy above 28 GPa (*9*, *11*, *13*, *18*). Further, previous results suggest highly divergent production of Fe_2O_3 in silicate liquids equilibrated with Fe-rich alloy. For example, theoretical calculations (*12*) predict that for Earth, core formation in a magma ocean at 30 GPa would yield a mantle in which 4 to 7% of the iron is Fe_2O_3, whereas extrapolation of existing experimental results suggests ratios of 70% (*11*) or 35 ± 15% (*13*). Here, we present silicate melt–Fe-rich alloy melt equilibration experiments conducted at pressures relevant to core formation in Earth-sized planets to investigate the production of Fe_2O_3 in a deep magma ocean and the initial oxidation state of the early Earth's mantle.

The team conducted laser-heated diamond anvil cells (LH-DACs) experiments at 3800 to 4200 K and 30 to 70 GPa on basaltic silicate melts, which were equilibrated with molten PtFe alloy. Experimental conditions are listed in table S1, and a range of PtFe alloy compositions were used to vary fO_2's. The compositions of the quenched basaltic silicate and Fe-alloy melts were analyzed by electron probe microanalyzer (EPMA), and the $Fe^{3+}/\Sigma Fe$ of the quenched silicate glass was analyzed by energy-domain synchrotron Mössbauer spectroscopy (E-SMS) at beamline ID18 at the European Synchrotron Radiation Facility (ESRF). Measured $Fe^{3+}/\Sigma Fe$ ratios ($Fe^{3+}/\Sigma Fe_m$) have been corrected using a recoilless fraction determined for basalt glasses [(*19*) and table S1] and are denoted as $Fe^{3+}/\Sigma Fe_c$ ratios.

RESULTS

Experiments produced molten PtFe alloy spheres with 7.4 to 38.4 atomic % Fe, surrounded by silicate melt, quenched to glasses with 14.8 to 31.7 weight % (wt %) FeO* and 40.1 to 31.8 wt % SiO_2 (tables S2 and S3). Glasses are homogenous at the spatial resolution of the EPMA analyses, without resolvable compositional (Soret) diffusion profiles [(*20*) and Fig. 1]. Alloy nanoparticles are absent or sufficiently sparse to be avoided during SMS analyses (fig. S1). The calculated fO_2 in experiments, derived from silicate-alloy equilibrium using thermodynamic models of FeO in quenched silicate (*10*) and Fe in PtFe alloy (*21*) range from IW −0.4 to +0.8, where IW refers to the iron wüstite reference oxygen buffer [(*22*) and table S1]. The disproportionation reaction

$$3FeO^{melt} = Fe^{alloy} + Fe_2O_3{}^{melt} \quad (1)$$

is the source of the ferric iron created in our experiments.

[1]State Key Laboratory of Geological Processes and Mineral Resources, China University of Geosciences, Beijing 100083, China. [2]Department of Earth Sciences, University of Minnesota, Minneapolis, MN 55455, USA. [3]School of Earth Sciences, University of Bristol, Bristol BS81RJ, UK. [4]ESRF–The European Synchrotron, CS40220, 38043 Grenoble Cedex 9, France. [5]Research School of Earth Sciences, Australian National University, Canberra, Australia. [6]National Museum of Natural History, Smithsonian Institution, Washington, DC 20560, USA. [7]Earth and Planets Laboratory, Carnegie Institution for Science, Washington, DC 20015, USA.
*Corresponding author. Email: zhanghl@cugb.edu.cn

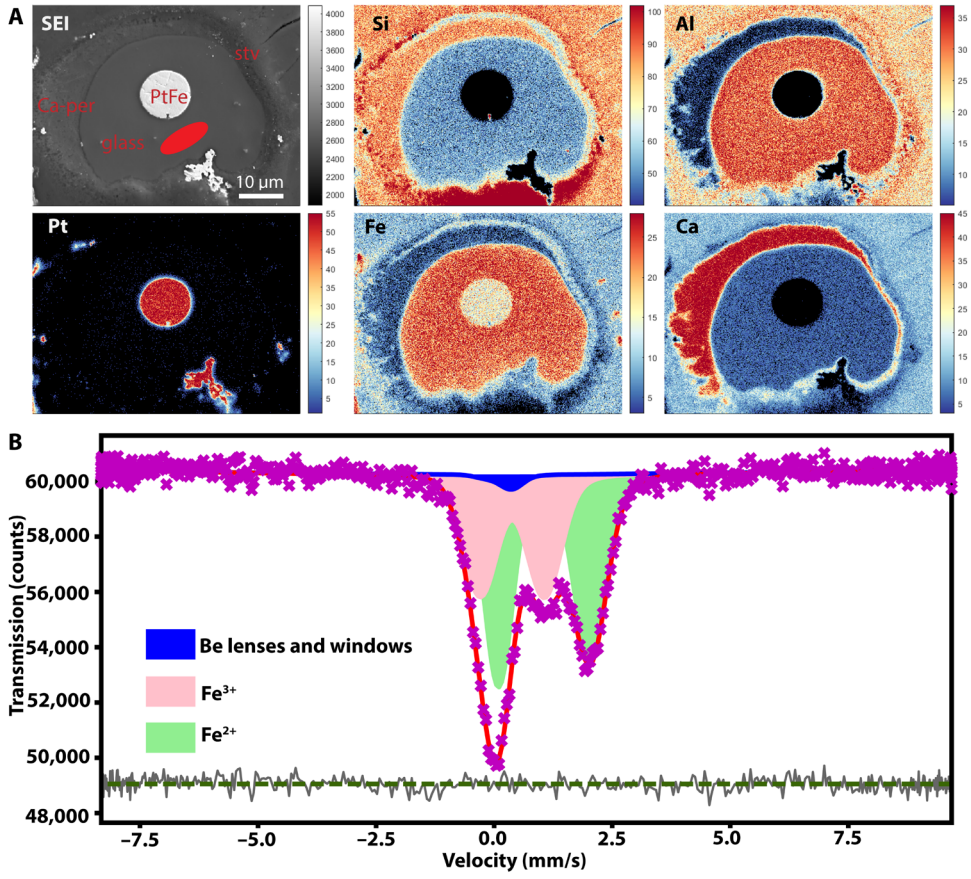

Fig. 1. Experiment DAC 93 (43.4 GPa, 3802 ± 93 K): Secondary electron image and elemental maps and E-SMS spectrum of quenched silicate glass. (**A**) EPMA wavelength dispersive spectrometry (WDS) elemental maps of Si, Al, Ca, Pt, and Fe together with an secondary electron image (SEI) of DAC 93, showing the very light grey PtFe alloy in the center and chemically homogeneous region of melt quenched to glass (dark gray). The color bars at each map right are counts. The homogeneous glass is surrounded by cooler regions that quenched Ca-perovskite (Ca-per) and stishovite (stv). The red ellipse in the SEI image represents the size and position of the 3.5 × 11–μm x-ray beam used for E-SMS analyses. (**B**) the E-SMS spectrum of quenched silicate glass of DAC 93 consists of one asymmetric doublet from the beamline optics (Fe impurities in Be lenses and windows) and one symmetric and asymmetric Voigt doublet from paramagnetic Fe^{3+} and Fe^{2+}, respectively.

E-SMS spectra of quenched silicate glasses consist of two broadened doublets derived from paramagnetic Fe^{2+} and Fe^{3+} (Fig. 1B). $Fe^{3+}/\Sigma Fe_m$ and $Fe^{3+}/\Sigma Fe_c$ ratios, resolved hyperfine parameters [center shifts (CSs) and quadrupole splittings (QSs)] are given in table S1 and data S1). The accuracy of these values was evaluated by analyzing four secondary standard mafic glasses quenched from experiments at 100 kPa to 5.5 GPa (data S2), which were analyzed previously by conventional Mössbauer spectroscopy [CMS; (*9*, *23*)]. Details of these experiments, their analyses, the effects of using different software packages, and assumptions about peak shapes to resolve $Fe^{3+}/\Sigma Fe_m$ ratios can be found in the Supplementary Materials. The $Fe^{3+}/\Sigma Fe_m$ ratios determined for the secondary standard mafic glasses by CMS and E-SMS agree within uncertainties, with the absolute values differing by an average of 0.008 ± 0.007 (fig. S2).

Resolved hyperfine parameters are similar to those observed previously for glasses quenched at 100 kPa or quenched from high pressure (up to 8 GPa) but analyzed after relaxation to 100 kPa (fig. S3) and are consistent with Fe^{2+} and Fe^{3+} in high spin octahedral coordination. No trends in hyperfine parameters with pressure that would possibly indicate a change in the bonding environment are apparent in the decompressed glasses (fig. S4). $Fe^{3+}/\Sigma Fe_c$ ratios range from 0.20 ± 0.01 to 0.44 ± 0.01 and do not show a strong pressure dependence (Fig. 2). The trend has some scatter, partly because of the effects of variable log fO_2, temperature, and bulk composition.

We used experimental determinations from this study, combined with earlier results from experiments that quenched to glasses (*9*, *11*, *18*), to refine a previous thermodynamic model (*10*, *12*) for the prediction of $Fe^{3+}/\Sigma Fe$ ratios of silicate melts as a function of composition, temperature, pressure, and fO_2 (see Supplementary Materials and Fig. 2). Because mismatches between the experiments and the previous fourth order Birch-Murnaghan model [(*10*, *12*) and fig. S5] are small and the compositional and temperature variations among all experiments are distributed unevenly, we refined only parameters that affect the pressure dependence, as documented in the Supplementary Materials. As listed in table S4, we explored multiple fitting strategies, making sure to avoid overfitting. The preferred model incorporates values from this study for the bulk modulus, K, and its pressure derivative K' ("fit 1" in table S4) and reproduces the experimental $Fe^{3+}/\Sigma Fe_c$ ratios with an average difference of 0.05.

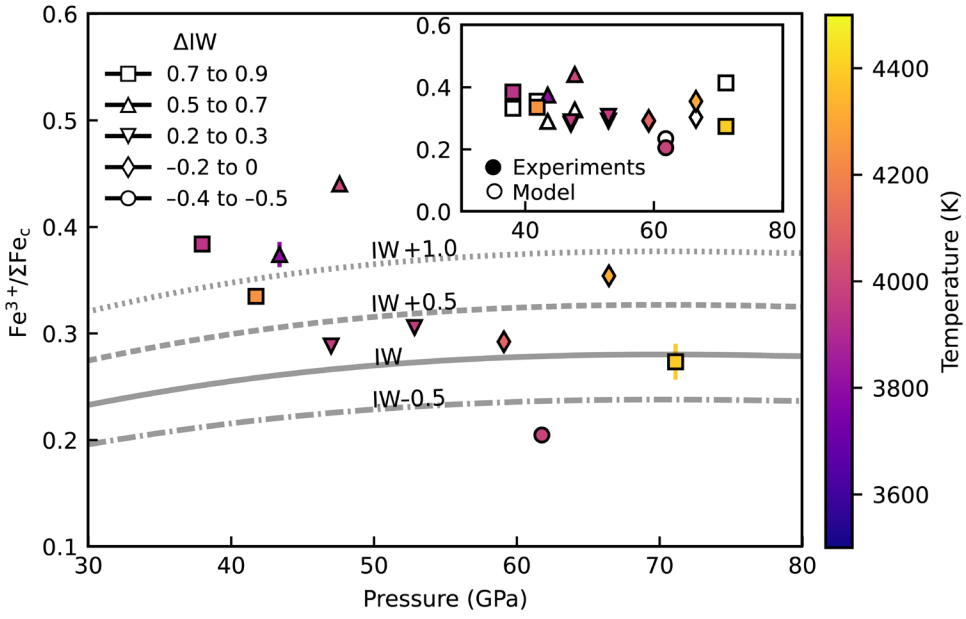

Fig. 2. $Fe^{3+}/\Sigma Fe_c$ ratios of silicate melts quenched from LH-DAC experiments, determined by E-SMS. $Fe^{3+}/\Sigma Fe_c$ ratios are resolved from E-SMS using SYNCmoss (*61*) and corrected for the effects of the recoilless free fraction following Zhang *et al.* [(*19*); correction factor, $C = 1.125$]. Different symbols refer to different fO_2's relative to IW (*22*), and symbol colors indicate experimental temperatures. The curves are calculated from the thermodynamic model (fit 1; table S4) with equation S18 at 4000 K using a silicate composition derived from the average of the experimental glasses at IW −0.5, IW, IW +0.5, and IW +1.0. Note that the curves presented here are for a single melt composition and temperature and therefore do not fully capture the variations observed in the experiments, which have variable melt compositions and temperatures. The inset shows the consistency between the $Fe^{3+}/\Sigma Fe_c$ ratios obtained from experiments and those calculated using our model (fit 1).

DISCUSSION

In contrast to low pressure (100 kPa) conditions, where silicate melts at IW −0.4 to +0.8 have small $Fe^{3+}/\Sigma Fe$ ratios [e.g., 0.03 to 0.06 (*15*) or 0.06 to 0.09 (*10*) at 2000 K], the $Fe^{3+}/\Sigma Fe_c$ ratios for high pressure melts from 38 to 71 GPa are much larger (0.20 to 0.45). Thus, the LH-DAC experiments confirm that equilibration with liquid Fe alloy at pressures similar to core segregation in deep magma oceans can produce appreciable oxidized iron, as originally proposed by Hirschmann (*8*) and as shown by previous high-pressure experiments (*11*, *13*) and first-principles calculations (*12*).

Given the comparatively oxidized conditions of the LH-DAC experiments, the observed $Fe^{3+}/\Sigma Fe_c$ ratios suggest moderate stabilization of Fe_2O_3 at pressures and fO_2 applicable to alloy-silicate equilibration in a deep terrestrial magma ocean (Fig. 2). The $Fe^{3+}/\Sigma Fe_c$ ratios are substantially lower than the enrichments expected based on extrapolation of the experiments of Armstrong *et al.* (*11*) and Kuwahara *et al.* (*13*) and are of a similar magnitude to values predicted by the first principles equations of state (EOS) with 12.5 mole % (mol %) FeO calculated by Deng et al. (*12*), but are greater than the first principles EOS with 25 mol % FeO from Deng *et al.* (*12*). Our data together with our model ('fit 1') show that, for iso-fO_2 and isothermal conditions, the $d(Fe^{3+}/\Sigma Fe)/dP$ slope levels off over the pressure range investigated (38–71 GPa, Fig. 2).

$Fe^{3+}/\Sigma Fe$ ratios calculated with our thermodynamic model reproduce $Fe^{3+}/\Sigma Fe_c$ ratios observed in glasses quenched from low-pressure (<8 GPa) experiments with a maximum difference of 0.09 (data S3 and fig. S6). For the high-pressure LH-DAC experiments at ≥38 GPa, the model reproduces $Fe^{3+}/\Sigma Fe_c$ ratios with an average and maximum difference of 0.075 and 0.15, respectively (data S1 and fig. S6). Conversely, the model predicts ratios notably lower (by as much as 0.47) than intermediate-pressure (10 to 28 GPa) experiments that produced crystalline quench products rather than glasses (data S3). The conversion of melt to quenched crystals may have compromised these experiments, either owing to disproportionation during quench or by creating challenges to the accurate spectroscopic characterization of $Fe^{3+}/\Sigma Fe_m$ in the resulting complex phase assemblages. Future studies producing glasses quenched between 7 and 35 GPa are needed to better characterize iron redox in silicate melts at these conditions.

Our revised thermodynamic model allows the calculation of $Fe^{3+}/\Sigma Fe$ ratios in a well-mixed magma ocean as a function of the mean pressure of silicate-alloy equilibration (Fig. 3). For silicate-alloy equilibration along magma ocean geotherms [see the Supplementary Materials and (*24*)], calculated $Fe^{3+}/\Sigma Fe$ ratios increase with depth. The disproportionation reaction (Eq. 1) is the source of Fe^{3+} in the deep magma ocean. The calculated $Fe^{3+}/\Sigma Fe$ ratios with our model (fit 1) are much lower than implied by using a third-order Tait EOS from Armstrong *et al.* (*11*) or Kuwahara *et al.* (*13*), greater than predicted by the fourth-order Birch-Murnaghan EOS from Deng *et al.* (*12*) and similar to but slightly greater than those calculated from the model of Hirschmann (*10*), which uses the EOS of Deng *et al.* (*12*) (Fig. 3).

At plausible mean pressures of equilibration between the magma ocean and core-destined molten alloy [28 to 53 GPa (*10*)], the predicted $Fe^{3+}/\Sigma Fe$ ratios range from 0.056 to 0.101 for the low-temperature (T_0 = 2100 K) geotherm and 0.070 to 0.112 for the high-temperature (T_0 = 2500 K) geotherm of Stixrude *et al.* [fig. S7 and (*24*)]. These values span the $Fe^{3+}/\Sigma Fe$ ratios (0.075 to 0.115; see the Supplementary Materials) needed to account for the redox budget (*25*, *26*) of the bulk silicate Earth [BSE; (*3*, *10*)] (Fig. 3). Therefore,

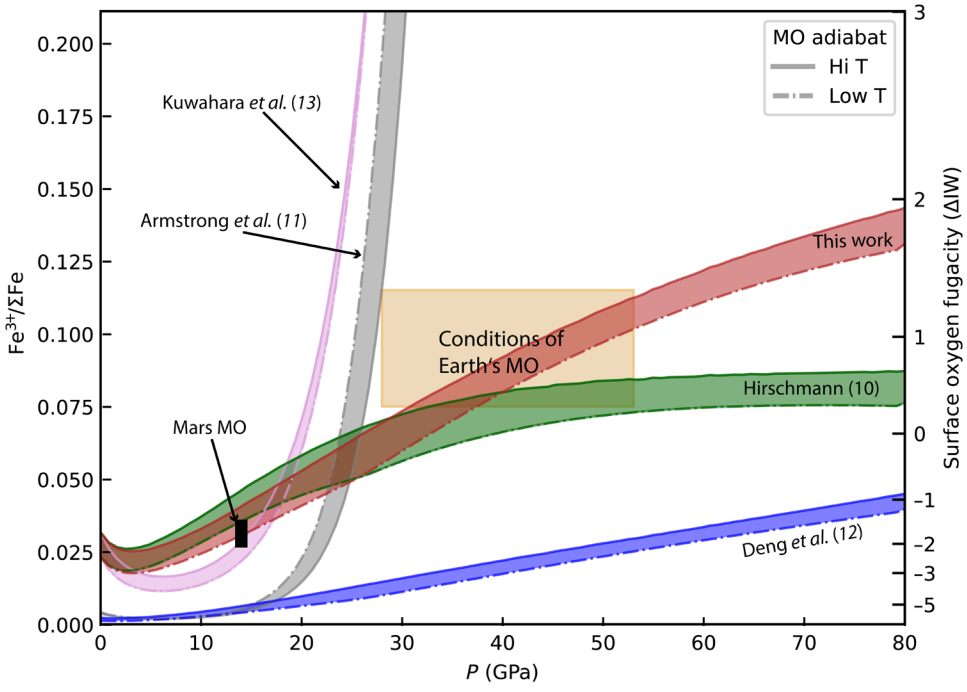

Fig. 3. $Fe^{3+}/\Sigma Fe$ ratios of Earth's magma ocean generated during and just after core formation as a function of pressure and surface magma ocean fO_2 relative to the IW buffer for those $Fe^{3+}/\Sigma Fe$ ratios. $Fe^{3+}/\Sigma Fe$ ratios (left *y* axis) of silicate melts in equilibrium with core-destined alloy for the bulk silicate composition of Earth (BSE) (*62*), as a function of pressure along two magma ocean (MO) adiabats using the thermodynamic model from this work (fit 1) and previous thermodynamic models (*10*–*12*), as well as interpolation of recent high pressure experiments to 28 GPa (*13*). The two MO adiabats (fig. S7; "Hi T": $T_0 = 2500$ K; "Low T": $T_0 = 2100$ K) are defined by Stixrude *et al.* (*24*). Along the MO adiabats, the log fO_2 set by metal-silicate equilibrium is calculated on the basis of the compositions of the silicate melt and liquid alloy and the thermodynamic properties of FeO and Fe in their respective melts, as detailed in the Supplementary Materials. The orange box shows the intersection of the mean depth of equilibration of metal and silicate in a terrestrial MO [from the compilation in (*10*)] and the range of $Fe^{3+}/\Sigma Fe$ of the MO required to account for the BSE redox budget ($Fe^{3+}/\Sigma Fe_{MO} = 0.095 \pm 0.02$; see the Supplementary Materials). Our model curve yields $Fe^{3+}/\Sigma Fe$ ratios of 0.056 to 0.112, which apply throughout the MO, while other models are either higher (*11*, *13*) or lower (*12*), except Hirschmann (*10*), which crosses the lower boundary. The right *y* axis shows the fO_2 at the MO surface, calculated at 100 kPa and 2273 K from the model of Hirschmann (*10*), based on the $Fe^{3+}/\Sigma Fe$ ratios displayed on the left *y* axis. Also shown is the calculated $Fe^{3+}/\Sigma Fe$ ratio applicable to Mars, with core forming conditions at 14 GPa, 2200 K, log fO_2 ranging from IW −1.5 to −1.1, and the silicate composition of bulk silicate Mars (*63*).

all of the present-day BSE redox budget may feasibly have originated by FeO disproportionation in Earth's liquid silicate magma ocean. Additional contributions from bridgmanite disproportionation (*1*) or hydrogen escape (*27*, *28*), tending to further oxidize the BSE, or late accretion, tending to reduce it (*3*, *27*), are not excluded, but their contributions may have been small or largely canceling.

The $Fe^{3+}/\Sigma Fe$ ratio in a well-mixed magma ocean influences the chemistry of the overlying atmosphere (*8*). With increasing mean depth of silicate-alloy equilibration, the magma ocean's $Fe^{3+}/\Sigma Fe$ ratio varies. At pressures above approximately 4 GPa, this results in an increase in fO_2 and CO_2/CO and H_2O/H_2 ratios in the atmosphere above the magma ocean (Fig. 4). Hotter silicate-alloy equilibration produces more Fe_2O_3 and therefore results in more oxidized surface conditions. Because different models (*10*, *15*) for the relationship between fO_2 and $Fe^{3+}/\Sigma Fe$ in peridotite melt disagree at moderately reducing conditions, two separate calculations are shown in Fig. 4, i.e., the model by Hirschmann (*10*) and the model by Sossi *et al.* (*15*). When applying pressure and temperature conditions plausible for a surficial magma ocean (2273 K and 100 kPa), both models however affirm that the predominant C and H species overlying a magma ocean equilibrated with alloy at 28 to 53 GPa [see review (*10*)] are, respectively, CO and H_2O. Because H_2O is far more soluble in silicate liquids than CO (or CO_2), the hot atmosphere above a terrestrial magma ocean will be dominated by CO, with much of the H_2O sequestered in the magma ocean itself (*29*, *30*). For Mars, liquid silicate–liquid alloy equilibration at a mean pressure of 14 GPa, 2200 K (*31*, *32*), and ΔIW = −1.5 to −1.1 (*10*) yield a $Fe^{3+}/\Sigma Fe$ ratio of 0.029 to 0.034 (Fig. 3). This would produce modestly reduced surface conditions [ΔIW = −1.31 to −0.91 (*10*) or ΔIW = −0.50 to −0.20 (*15*)] and an atmosphere rich in CO, H_2O, and possibly H_2 (Fig. 4). However, upon solidification of the Mars's magma ocean and oxidation of Cr^{2+} to Cr^{3+}, nearly all of the magma ocean's Fe_2O_3 would be eliminated (*10*), resulting in a highly reduced solidified mantle. Yet, this is incompatible with the modestly oxidized character of Martian igneous rocks [≥IW; (*33*)]. Possibly, the redox state of the Martian mantle was affected considerably by hydrogen escape from the magma ocean atmosphere, as evidenced by notable D/H enrichments in the Martian mantle (*34*). We note, however, that the EOS we use is not optimized at 14 GPa as it has been calibrated at higher pressure. In addition, the predictions for Martian magma ocean conditions are limited and have more uncertainty than for the terrestrial case.

LH-DAC experiments at 38 to 71 GPa affirm that Fe_2O_3 is stabilized in a deep magma ocean in equilibrium with liquid Fe alloy. On the basis of these results, an updated EOS for Fe oxides in silicate liquids reveals that the Fe_2O_3 generated in a terrestrial magma ocean

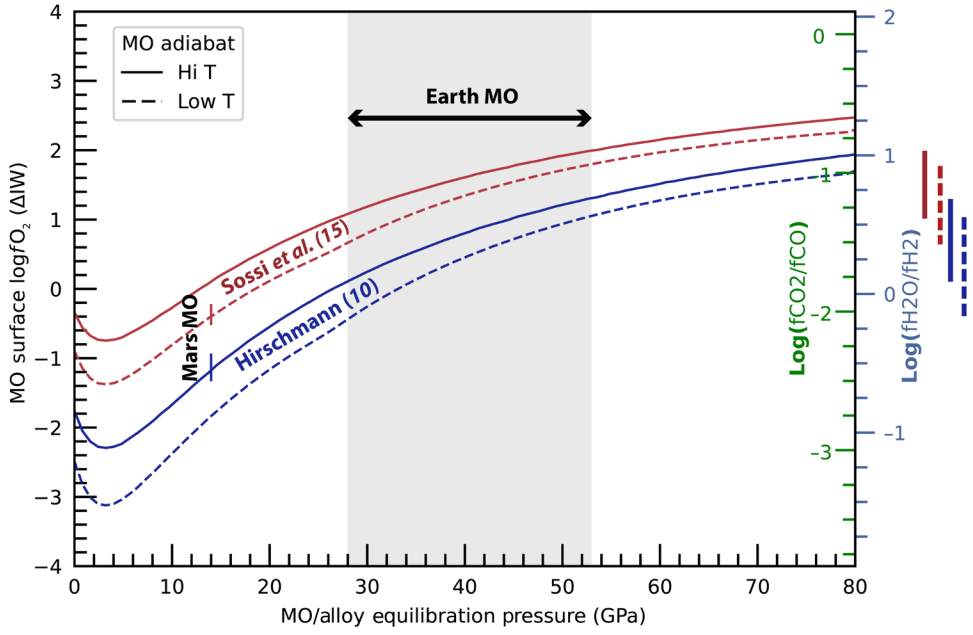

Fig. 4. logfO_2 at the surface of a terrestrial magma ocean as a function of the mean pressure of equilibration of the magma ocean with core-destined alloy and corresponding ratios of volatile species in the atmosphere [log(fCO$_2$/fCO) and log(fH$_2$O/fH$_2$)]. The fO_2 level at the surface of a magma ocean (MO) rises with increasing metal-silicate equilibration pressure because $Fe^{3+}/\Sigma Fe$ of the silicate melt increases in this pressure range (Fig. 3). In a well-mixed magma ocean, the $Fe^{3+}/\Sigma Fe$ ratio remains constant throughout the magma column. Accordingly, the H_2O/H_2 (light blue scale) and CO_2/CO (green scale) ratios (right *y* axis) of the overlying atmosphere also increase as the metal-silicate equilibration depth increases. High-temperature (T_0 = 2500 K) and low-temperature (T_0 = 2100 K) adiabats (*24*) are shown, with more oxidized conditions resulting for the hotter magma ocean geotherm. Two models (*10*, *15*) are used to convert $Fe^{3+}/\Sigma Fe$ in the magma ocean to surface log fO_2. Under reducing conditions, where large changes in fO_2 correspond to small variations in $Fe^{3+}/\Sigma Fe$, small differences in the two models convert to notably different fO_2 for the same $Fe^{3+}/\Sigma Fe$ ratios [see figure 9 in (*10*)]. The vertical gray band shows the expected mean pressures of equilibration for core formation on Earth, as in Fig. 3. Surface fO_2 and gas speciation are calculated using JANAF (*64*) for the indicated surface fO_2's on the left-hand *y* axis at pressure and temperature conditions plausible for a surficial magma ocean (2273 K and 100 kPa). The red and blue vertical lines on the right of the plot represent the ranges of surface logfO_2 and volatile species ratios that correspond to the pressure interval of Earth's magma ocean. Also shown are surface redox and atmospheric compositions calculated for Mars at 2000 K and 100 kPa.

with mean alloy-silicate equilibration pressures of 28 to 53 GPa could feasibly account for the entire BSE redox budget and would produce surface conditions ranging from IW −0.41 to +1.30 (*10*) or IW +0.68 to +1.98 (*15*), which would foster an atmosphere primarily composed of CO and H_2O.

MATERIALS AND METHODS

Starting materials

A basaltic composition similar to previous work (*23*) was used as the starting material and was prepared from reagent-grade oxides (SiO_2, Al_2O_3, Fe_2O_3, TiO_2, and MgO) and carbonates ($CaCO_3$, Na_2CO_3, and K_2CO_3). Before weighing, the oxides and carbonates were devolatilized following procedures as described by Zhang *et al.* (*9*). Appropriate proportions of these reagents were then ground in an agate mortar and pestle with ethanol for at least 1 hour until the grinding sound ceased and then devolatilized by firing at 1000°C for 48 hours with a heating rate of 100°C/hour. Last, the iron oxide, added as 100% $^{57}Fe_2O_3$, was mixed into the starting materials by grinding under ethanol, to analyze Fe^{3+} using E-SMS. The starting material was then reduced at 1000°C in a CO_2:CO atmosphere with fO_2 corresponding to the quartz-fayalite-magnetite (QFM) buffer for 12 hours.

The basaltic starting material was melted and rapidly quenched to a glass in a single experiment (B3) performed in an aerodynamic levitation furnace at the University of Bristol (UoB). A pressed cylindrical pellet of the starting material was first heated on a copper hearth using a Nd:yttrium-aluminum-garnet fiber laser until partial melting produced a sphere approximately 1 mm in diameter. The sphere was then levitated in flowing argon gas and heated using the same laser at a power of 30 W for 1 min to super liquidus conditions and quenched by switching off the power to the laser. The glass bead was then broken into several pieces, with three random pieces extracted and examined for homogeneity and chemical composition using back-scattered electron images and wavelength dispersive spectrometry (WDS) EPMA analyses. Details of the quantitative analyses of the basaltic starting composition are given in table S2. The remaining pieces were ground into powder under ethanol in an agate mortar for over 2 hours. A portion of the powder was mixed with powdered sugar for CMS, and the rest was pressed into ~15-μm glass powder discs with a tablet press.

Pt foil with a thickness of 2 μm (99.95%; Goodfellow) was cut into ~30- to 40-μm-diameter disks using a New Wave ultraviolet (UV) laser ablation system operating at a wavelength of 266 nm, a pulse frequency of 20 Hz, and a pulse width of 40 ns. Some of the discs were double coated with Fe of different thicknesses (0.286 μm for $Pt_{95}Fe_5$, 0.572 μm for $Pt_{90}Fe_{10}$, and 0.962 μm for $Pt_{85}Fe_{15}$, with subscripts referring to weight proportions) using a Quorum Q150T-ES magnetron sputter coater equipped with an Fe target of 99.95% purity (Goodfellow) to vary the redox conditions of the LH-DAC experiments.

Diamond anvil cell preparation

High-pressure experiments were performed in "Princeton-type" symmetric DACs using type I diamond anvils with culet diameters of 200 or 250 μm. Re and steel gaskets were pre-indented to 20 to 25 GPa and ~20 GPa, respectively. One sample chamber was drilled in each indentation with a diameter ~$^1/_3$ of the culet size using the UV laser ablation system described previously. All sample chambers were filled with two ~15-μm-thick glass power discs with one ~2-μm-thick PtFe alloy foil between them (fig. S8). The glass powder discs act as both thermal insulation and starting material, so no other potential contaminants were required. Before sealing and pressurizing, the loaded DAC was heated to ~120°C for about 1 hour to remove adsorbed water and then closed.

Pressure measurement

Pressure was determined on the basis of the Raman shift of the singlet peak related to stress in the (001) direction at the diamond culet surface (*35*) using the calibration relative to the ruby fluorescence scale of Mao *et al.* (*36*) presented in Baron *et al.* (*37*). Raman shifts were measured using a confocal Jobin Yvon T64000 Raman microscope with a spectral resolution of ~0.4 cm^{-1} and a diffraction-limited focal volume with a diameter of ~4 μm. For each experiment, the pressure was measured at the center of the culet before laser heating and directly on the heated spot after laser heating. Pre-heating and post-heating pressure measurements are reported in table S1. Only post-heating pressures have been used during the following thermodynamic fitting procedure. We do not correct for thermal pressure because we have not measured its magnitude in experiments with this specific geometry and composition. Previous experiments indicate that the thermal pressure in typical DAC experiments does not exceed ~10% of the pressure measured at room temperature (*38*, *39*).

Laser heating and temperature measurement

After compression, samples were heated using the double-sided laser heating system installed in the School of Earth Sciences, UoB. The system consists of two 100-W Yb-doped fiber lasers (λ =1070 nm) coupled with beam-shaping and beam-expanding optics to maximize the uniformity of the energy density while maximizing the size of the heated spot to minimize radial temperature gradients. The beam was aimed at the center of the PtFe foil. During the experiments, a specific heating protocol, referred to as "ramp mode," was implemented following Baron *et al.* (*37*). This mode entailed the incremental and automated increase of laser power by approximately 0.2 W on each side every 4 to 6 s, leading to a heating rate of 500 to 1500 K/min. Super-liquidus conditions were maintained for at least 30 s to ensure equilibration between the silicate glass and PtFe alloy (figs. S7 and S9). After that, the sample was quenched near-instantaneously by switching off the power to the lasers.

At each step during the laser heating, the sample temperature was measured using one-dimensional (1D) spectroradiometry (*40*) and 2D multispectral imaging radiometry [MIR; (*41*)]. Thermal emission spectra were simultaneously captured on both sides of the sample across a 2-μm-wide strip, covering a wavelength range of 570 to 830 nm. Temperatures were determined by normalizing the spectra to that of a NIST-calibrated W-lamp of known spectral radiance. Normalized sample spectra were fitted to the Wien approximation to the Planck function. To minimize the effects of chromatic aberration, a 200-μm bandpass was selected from each measured spectrum that minimized the average analytical error. The temperature precision during the fit was typically better than 10 K at 3000 K. To mitigate artifacts caused by the spatial resolution of the charge-coupled device (CCD) at the object plane (~1 μm) being smaller than the system's actual optical resolution (~3 μm), a boxcar smoothing procedure was implemented on all temperature profiles. Temperature cross sections measured from both sides of one experiment (DAC 93) are plotted versus time in fig. S9A. The temporally and spatially averaged temperatures ($T_{average}$) given in table S1 are those used as characteristic of sample conditions and for input into the thermodynamic models. Uncertainty in the accuracy of measured temperatures arise from the wavelength dependence of the sample emissivity. On the basis of measurements of the absorption properties of oxides and lower mantle silicates at high pressures and temperatures over the wavelength range used in this study for spectroradiometry and MIR, temperatures may be overestimated by several hundred degrees kelvin (*42*, *43*). However, the spectral emissivity of the silicate melts formed in our experiments at high temperatures have not been measured, and we do not correct our temperatures for this unknown effect. For a comprehensive understanding of the laser heating and temperature measurement system used in this study, including calibration, benchmarking, and uncertainties, we refer readers to the work of Lord *et al.* (*44*) and references therein.

2D temperature maps were acquired using four-color MIR. In this method, a ×50 magnified image of the sample is focused onto each quadrant of a CCD camera (SBIG Model ST-402ME) at four distinct wavelengths (579, 670, 753, and 851 nm). When spatially correlated, this leads to four wavelength-intensity data points at each pixel, which can be fitted using the Wien approximation to the Planck function to yield temperature and emissivity. All processing was performed on the fly with a spatial precision of ±1 pixel using the MIRRORS software package (*45*). The major advantage of MIR over 1D spectroradiometry is its ability to always capture the peak temperature of a sample, even when the hotspot is moving rapidly within a dynamic, super-liquidus sample. A 2D temperature map and error map of experiment DAC 93 is shown in fig. S9 (B and C), and the peak temperatures measured during heating are shown in movie S1.

Decompressed sample preparation

To obtain the $Fe^{3+}/\Sigma Fe_m$ ratios in samples decompressed from DAC experiments, it is essential to expose both sides of the heated spot. The minimum beam size of our synchrotron Mossbauer spectroscopy measurements was 3 × 7 μm at ID18 at ESRF and generally is 4 × 11 μm (*46*). Therefore, the larger the area exposed on both sides of the heated area, the better. Thus, the following steps were performed and illustrated in fig. S10:

1) The culet regions of decompressed gaskets were cut out with the same UV laser ablation system described previously.

2) The cut-out culet was placed on a flat surface, surrounded with a 1-inch mold, and back-filled with epoxy.

3) The cured epoxy was polished to expose the heated glass area using 1500, 3000, and 4000-grit polishing pads. During this process, it was possible to visually verify whether the PtFe metal ball was in the glass pool. If the PtFe metal ball was present, then polishing continued with 1-μm Buehler diamond suspension until the metal ball was exposed. Only experiments with PtFe balls are reported.

4) Successfully polished samples were coated with carbon and analyzed using a JEOL JXA8530F Field Emission Gun EPMA.

5) After the EPMA analyses, the sample was remounted in epoxy as in step two, polished side upward. After curing, most of the old epoxy was cut away with a blade saw.

6) The old left epoxy and the new cured epoxy were then polished to expose the second side of the heated glass pool; the double polished samples' thickness is ~5 μm.

7) The back epoxy was polished down to a 1 mm in thickness.

Piston cylinder experiments

For E-SMS analyses, we examined secondary standard glasses for which $Fe^{3+}/\Sigma Fe_m$ had also been determined by CMS. These came from the study of Zhang *et al.* (*9*), but one additional glass not previously reported was also used. This glass, with the same andesitic composition as those described by Zhang *et al.* (*9*), was produced to yield a composition in which all the iron was Fe^{3+}. The glass (End3+) was made in a piston cylinder (PC) experiment conducted at 3 GPa, 1400°C for 2 hours. Fe for this material was added as Fe_2O_3, consisting of 70% normal reagent oxide and 30% $^{57}Fe_2O_3$ (Isoflex Inc.). The starting material together with about 10 wt % PtO_2 was placed in a 2-mm-diameter Pt capsule as two layers. The experiment was performed in a half-inch, end-loaded PC apparatus at the University of Minnesota, Twin Cities. The assemblies and pressure calibrations are reported by Xirouchakis *et al.* (*47*), and the temperature was measured using a type B thermocouple ($Pt_{70}Rh_{30}$/$Pt_{94}Rh_6$), with calibrations by Zhang and Hirschmann (*48*). The quenched glass was extracted from the capsule, and random pieces were selected and double-polished for optical examination, EPMA, and E-SMS analysis. The remainder was ground to powder and mixed with sugar for CMS.

EPMA

Sample textures were examined by backscatter electron and secondary electron imaging. Major element concentrations of quenched glasses and PtFe alloys were determined by WDS using JEOL JXA8530F EPMAs at UoB and at the University of Science and Technology of China (USTC). A focused beam with an acceleration voltage of 15 kV and a beam current of 10 nA was used. Counting times were 20 and 10 s for peak and background, respectively, for both standard analyses and unknown samples. Data were acquired using the following diffractometer crystals: LiFH for Fe Kα; PETJ for K Kα and Ca Kα; PETL for Ti Kα and Pt Lα; and TAP for Al Kα, Mg Kα, Si Kα, and Na Kα (TAPH for Na and Al at UoB). Mineral and glass standards—including albite for Si, Na, and Al; TiO_2 for Ti; magnetite (USTC) and fayalite (UoB) for Fe; sanidine for K; wollastonite (UoB) and diopside (USTC) for Ca; and olivine for Mg from Jarosewich *et al.* (*49*)—were chosen on the basis of an analysis of secondary glass standards. Pure Fe and Pt metals were used as standards to analyze the PtFe alloys. Si was also analyzed to ensure the beam was on the alloy. Matrix corrections were computed with probe for EPMA software. United States Geological Survey glasses BCR-2G (*50*) and in house glasses 3570 at UoB (*51*) were analyzed as secondary standards before sample analysis sessions. The intensity data of standards, secondary standards, and unknown samples were checked for time-dependent intensity (TDI) changes with probe for EPMA software, and values for Si Kα and Na Kα were corrected using a self-calibrated function; no TDI effect was detected for other elements. The compositions of silicate glasses and PtFe alloys from the LH-DAC experiments, B3, and secondary standards are listed in tables S2 and S3.

Conventional Mössbauer spectroscopy

CMS of starting basaltic glasses (B3) were collected using a constant acceleration Ranger spectrometer at the Institute for Rock Magnetism, University of Minnesota, and the measurements were carried out with a ^{57}Co/Rh source and a pure Fe foil calibrant at room temperature (293 K). Data were collected over 512 channels and then folded to produce 256 unique channels. All spectra were collected over at least 1 day until sufficient (>1,000,000) counts per channel were accumulated to minimize statistical error. Sample mounts consisted of powdered glass mixed with powdered sugar evenly distributed in an approximately circular shape with a diameter of 12.7 mm. The absorber thickness was adjusted for an Fe density of 2 mg/cm^2.

The B3 spectrum has broadened line shapes typical of silicate glasses (*9*, *18*, *52*–*57*) and was fitted with a 2D distribution extended Voigt-based fitting (xVBF) method with the RECOIL software package (*58*) following Zhang *et al.* (*56*), and hyperfine parameters and their 1 sigma SD estimations are listed in data S2.

Energy-domain synchrotron Mössbauer source

E-SMS spectra of the double polished LH-DAC samples plus secondary standards, including the four glasses from low-pressure (<8 GPa) experiments previously analyzed (*9*) and sample End3+ synthesized in this study, were collected at beamline ID18 of the ESRF (*46*, *59*) with the storage ring operated in 7/8+1 mode with a mean current of 196 mA. The synchrotron beam was monochromatized to a bandwidth of ~10 neV at the ^{57}Fe resonant energy by a $^{57}FeBO_3$ single crystal with a beam size of 3.5 × 11 μm using Kirkpatrick-Baez mirrors. The crystal monochromator oscillated in a sinusoidal mode for Doppler effect absorption measurements over a range of energies. Source velocity was calibrated with an α-Fe foil. To assess if ferromagnetic sextets were present, the velocity scale was set to ±9 mm/s. The standard single-line Mössbauer absorber, $K_2Mg^{57}Fe(CN)_6$, was used to check the stability of the source instrumental function before and after each sample measurement.

During the analysis of DAC experiments by E-SMS, pools of glass were identified by comparison to optical and backscatter electron images of both sides of the double-polished samples collected by EPMA. Each E-SMS analysis of glass was conducted as close to the central alloy ball as possible, without spectral evidence of overlap from metallic Fe in the quenched alloy. To distinguish glass spectra from those possibly contaminated by neighboring phases, one analysis was conducted deliberately on the boundary between glass and PtFe alloy, and another was collected on the boundary between glass and crystalline silicate.

All E-SMS spectra at ID18 include an asymmetric doublet from Fe contamination in beamline optics (Be lenses and windows). This doublet was fit in all spectra with fixed hyperfine parameters derived from an earlier background measurement at ID18.

We explored three different methods for fitting the E-SMS spectra:

1) xVBF_MossA: Uses the xVBF method following Zhang *et al.* (*56*) using the MossA software package (*60*).

2) VBF_xVBF: Uses the VBF method for Fe^{3+} and xVBF for Fe^{2+} using the MossA software package (*60*).

3) SYNCmoss: Uses Voigt lineshape for Fe^{3+} and a line width ratio method, incorporating the Gaussian distribution with a linear

correlation between hyperfine parameters (CS and QS) for Fe^{2+} as implemented in the SYNCmoss software package (*61*).

In the Supplementary Text, we compare these and evaluate which method is preferable for quantifying the LH-DAC glass analyses.

Supplementary Materials

The PDF file includes:

Supplementary Text
Figs. S1 to S14
Tables S1 to S4
Legend for movie S1
Legends for data S1 to S5
References

Other Supplementary Material for this manuscript includes the following:

Movie S1
Data S1 to S5

REFERENCES AND NOTES

1. D. J. Frost, C. A. McCammon, The redox state of Earth's mantle. *Annu. Rev. Earth Planet. Sci.* **36**, 389–420 (2008).
2. B. Scaillet, F. Gaillard, Redox state of early magmas. *Nature* **480**, 48–49 (2011).
3. M. M. Hirschmann, The deep Earth oxygen cycle: Mass balance considerations on the origin and evolution of mantle and surface oxidative reservoirs. *Earth Planet. Sci. Lett.* **619**, 118311 (2023).
4. J. W. Keefner, S. J. Mackwell, D. L. Kohlstedt, F. Heidelbach, Dependence of dislocation creep of dunite on oxygen fugacity: Implications for viscosity variations in Earth's mantle. *J. Geophys. Res.* **116**, B05201 (2011).
5. V. Stagno, Y. Fei, The redox boundaries of earth's interior. *Elements* **16**, 167–172 (2020).
6. F. Gaillard, F. Bernadou, M. Roskosz, M. A. Bouhifd, Y. Marrocchi, G. Iacono-Marziano, M. Moreira, B. Scaillet, G. Rogerie, Redox controls during magma ocean degassing. *Earth Planet. Sci. Lett.* **577**, 117255 (2022).
7. D. J. Frost, U. Mann, Y. Asahara, D. C. Rubie, The redox state of the mantle during and just after core formation. *Philos. Trans. A Math. Phys. Eng. Sci.* **366**, 4315–4337 (2008).
8. M. M. Hirschmann, Magma ocean influence on early atmosphere mass and composition. *Earth Planet. Sci. Lett.* **341**, 48–57 (2012).
9. H. L. Zhang, M. M. Hirschmann, E. Cottrell, A. C. Withers, Effect of pressure on $Fe^{3+}/\Sigma Fe$ ratio in a mafic magma and consequences for magma ocean redox gradients. *Geochim. Cosmochim. Acta* **204**, 83–103 (2017).
10. M. M. Hirschmann, Magma oceans, iron and chromium redox, and the origin of comparatively oxidized planetary mantles. *Geochim. Cosmochim. Acta* **328**, 221–241 (2022).
11. K. Armstrong, D. J. Frost, C. A. McCammon, D. C. Rubie, T. Boffa Ballaran, Deep magma ocean formation set the oxidation state of Earth's mantle. *Science* **365**, 903–906 (2019).
12. J. Deng, Z. X. Du, B. B. Karki, D. B. Ghosh, K. K. M. Lee, A magma ocean origin to divergent redox evolutions of rocky planetary bodies and early atmospheres. *Nat. Commun.* **11**, 2007 (2020).
13. H. Kuwahara, R. Nakada, S. Kadoya, T. Yoshino, T. Irifune, Hadean mantle oxidation inferred from melting of peridotite under lower-mantle conditions. *Nat. Geosci.* **16**, 461–465 (2023).
14. N. Katyal, G. Ortenzi, J. Lee Grenfell, L. Noack, F. Sohl, M. Godolt, A. García Muñoz, F. Schreier, F. Wunderlich, H. Rauer, Effect of mantle oxidation state and escape upon the evolution of Earth's magma ocean atmosphere. *Astron. Astrophys.* **643**, A81 (2020).
15. P. A. Sossi, A. D. Burnham, J. Badro, A. Lanzirotti, M. Newville, H. St, C. O'Neill, Redox state of Earth's magma ocean and its Venus-like early atmosphere. *Sci. Adv.* **6**, eabd1387 (2020).
16. T. Lichtenberg, J. Drążkowska, M. Schönbächler, G. J. Golabek, T. O. Hands, Bifurcation of planetary building blocks during Solar System formation. *Science* **371**, 365–370 (2021).
17. A. Boujibar, P. Driscoll, Y. Fei, Super-Earth internal structures and initial thermal states. *J. Geophys. Res. Planets* **125**, e2019JE006124 (2020).
18. H. St, C. O'Neill, A. J. Berry, C. McCammon, K. D. Jayasuriya, S. J. Campbell, G. Foran, An experimental determination of the effect of pressure on the $Fe^{3+}/\Sigma Fe$ ratio of an anhydrous silicate melt to 3.0 GPa. *Am. Mineral.* **91**, 404–412 (2006).
19. H. L. Zhang, E. Cottrell, P. A. Solheid, K. A. Kelley, M. M. Hirschmann, Determination of $Fe^{3+}/\Sigma Fe$ of XANES basaltic glass standards by Mössbauer spectroscopy and its application to the oxidation state of iron in MORB. *Chem. Geol.* **479**, 166–175 (2018).
20. R. Sinmyo, K. Hirose, The Soret diffusion in laser-heated diamond-anvil cell. *Phys. Earth Planet. Inter.* **180**, 172–178 (2010).
21. M. M. Hirschmann, H. L. Zhang, A revised model for activity–composition relations in solid and molten FePt alloys and a preliminary model for characterization of oxygen fugacity in high-pressure experiments. *Eur. J. Mineral.* **35**, 789–803 (2023).
22. M. M. Hirschmann, Iron-wüstite revisited: A revised calibration accounting for variable stoichiometry and the effects of pressure. *Geochim. Cosmochim. Acta* **313**, 74–84 (2021).
23. E. Cottrell, K. A. Kelley, A. Lanzirotti, R. A. Fischer, High-precision determination of iron oxidation state in silicate glasses using XANES. *Chem. Geol.* **268**, 167–179 (2009).
24. L. Stixrude, N. de Koker, N. Sun, M. Mookherjee, B. B. Karki, Thermodynamics of silicate liquids in the deep Earth. *Earth Planet. Sci. Lett.* **278**, 226–232 (2009).
25. K. A. Evans, Redox decoupling and redox budgets: Conceptual tools for the study of earth systems. *Geology* **34**, 489 (2006).
26. K. A. Evans, The redox budget of subduction zones. *Earth Sci. Rev.* **113**, 11–32 (2012).
27. K. J. Zahnle, M. Gacesa, D. C. Catling, Strange messenger: A new history of hydrogen on Earth, as told by Xenon. *Geochim. Cosmochim. Acta* **244**, 56–85 (2019).
28. E. D. Young, A. Shahar, H. E. Schlichting, Earth shaped by primordial H_2 atmospheres. *Nature* **616**, 306–311 (2023).
29. M. M. Hirschmann, Constraints on the early delivery and fractionation of Earth's major volatiles from C/H, C/N, and C/S ratios. *Am. Mineral.* **101**, 540–553 (2016).
30. P. A. Sossi, P. M. E. Tollan, J. Badro, D. J. Bower, Solubility of water in peridotite liquids and the prevalence of steam atmospheres on rocky planets. *Earth Planet. Sci. Lett.* **601**, 117894 (2023).
31. N. Rai, S. Ghosh, M. Wälle, W. van Westrenen, Quantifying the effect of solid phase composition and structure on solid–liquid partitioning of siderophile and chalcophile elements in the iron–sulfur system. *Chem. Geol.* **357**, 85–94 (2013).
32. K. Righter, R. Rowland, L. R. Danielson, M. Humayun, S. Yang, N. Mayer (Waeselmann), K. Pando, Mantle–melt partitioning of the highly siderophile elements: New results and application to Mars. *Meteorit. Planet. Sci.* **55**, 2741–2757 (2020).
33. M. E. Schmidt, C. M. Schrader, T. J. McCoy, The primary fO_2 of basalts examined by the Spirit rover in Gusev Crater, Mars: Evidence for multiple redox states in the martian interior. *Earth Planet. Sci. Lett.* **384**, 198–208 (2013).
34. K. Pahlevan, L. Schaefer, L. T. Elkins-Tanton, S. J. Desch, P. R. Buseck, A primordial atmospheric origin of hydrospheric deuterium enrichment on Mars. *Earth Planet. Sci. Lett.* **595**, 117772 (2022).
35. M. Hanfland, K. Syassen, S. Fahy, S. G. Louie, M. L. Cohen, The first-order Raman mode of diamond under pressure. *Phys. B+C* **139–140**, 516–519 (1986).
36. H. K. Mao, J. Xu, P. M. Bell, Calibration of the ruby pressure gauge to 800 kbar under quasi-hydrostatic conditions. *J. Geophys. Res.* **91**, 4673–4676 (1986).
37. M. A. Baron, O. T. Lord, R. Myhill, A. R. Thomson, W. Wang, R. G. Trønnes, M. J. Walter, Experimental constraints on melting temperatures in the $MgO–SiO_2$ system at lower mantle pressures. *Earth Planet. Sci. Lett.* **472**, 186–196 (2017).
38. G. Fiquet, A. L. Auzende, J. Siebert, A. Corgne, H. Bureau, H. Ozawa, G. Garbarino, Melting of peridotite to 140 gigapascals. *Science* **329**, 1516–1518 (2010).
39. D. Andrault, N. Bolfan-Casanova, G. L. Nigro, M. A. Bouhifd, G. Garbarino, M. Mezouar, Solidus and liquidus profiles of chondritic mantle: Implication for melting of the Earth across its history. *Earth Planet. Sci. Lett.* **304**, 251–259 (2011).
40. M. J. Walter, K. T. Koga, The effects of chromatic dispersion on temperature measurement in the laser-heated diamond anvil cell. *Phys. Earth Planet. Inter.* **143–144**, 541–558 (2004).
41. A. J. Campbell, Measurement of temperature distributions across laser heated samples by multispectral imaging radiometry. *Rev. Sci. Instrum.* **79**, 015108 (2008).
42. J. Deng, Z. Du, L. R. Benedetti, K. K. M. Lee, The influence of wavelength-dependent absorption and temperature gradients on temperature determination in laser-heated diamond-anvil cells. *J.Appl. Phys.* **121**, 025901 (2017).
43. S. S. Lobanov, N. Holtgrewe, G. Ito, J. Badro, H. Piet, F. Nabiei, J.-F. Lin, L. Bayarjargal, R. Wirth, A. Schreiber, A. F. Goncharov, Blocked radiative heat transport in the hot pyrolitic lower mantle. *Earth Planet. Sci. Lett.* **537**, 116176 (2020).
44. O. T. Lord, E. T. H. Wann, S. A. Hunt, A. M. Walker, J. Santangeli, M. J. Walter, D. P. Dobson, I. G. Wood, L. Vočadlo, G. Morard, M. Mezouar, The NiSi melting curve to 70GPa. *Phys. Earth Planet. Inter.* **233**, 13–23 (2014).
45. O. T. Lord, W. Wang, MIRRORS: A MATLAB® GUI for temperature measurement by multispectral imaging radiometry. *Rev. Sci. Instrum.* **89**, 104903 (2018).
46. V. Potapkin, A. I. Chumakov, G. V. Smirnov, J.-P. Celse, R. Rüffer, C. McCammon, L. Dubrovinsky, The ^{57}Fe synchrotron Mössbauer source at the ESRF. *J. Synchrotron Radiat.* **19**, 559–569 (2012).
47. D. Xirouchakis, M. M. Hirschmann, J. Simpson, The effect of titanium on the silica content of mantle-derived melts. *Geochim. Cosmochim. Acta* **65**, 2201–2217 (2001).
48. Z. Zhang, M. M. Hirschmann, Experimental constraints on mantle sulfide melting up to 8 GPa. *Am. Mineral.* **101**, 181–192 (2016).
49. E. Jarosewich, J. A. Nelen, J. A. Norberg, Reference samples for electron microprobe analysis. *Geostand. Newsl.* **4**, 43–47 (1980).
50. K. P. Jochum, U. Nohl, K. Herwig, E. Lammel, B. Stoll, A. W. Hofmann, GeoReM: A new geochemical database for reference materials and isotopic standards. *Geostand. Geoanalytical Res.* **29**, 333–338 (2005).

51. E. C. Hughes, B. Buse, S. L. Kearns, J. D. Blundy, G. Kilgour, H. M. Mader, Low analytical totals in EPMA of hydrous silicate glass due to sub-surface charging: Obtaining accurate volatiles by difference. *Chem. Geol.* **505**, 48–56 (2019).
52. H. V. Alberto, J. L. Pinto da Cunha, B. O. Mysen, J. M. Gil, N. Ayres de Campos, Analysis of Mössbauer spectra of silicate glasses using a two-dimensional Gaussian distribution of hyperfine parameters. *J. Non Cryst. Solids* **194**, 48–57 (1996).
53. S. Rossano, E. Balan, G. Morin, J.-P. Bauer, G. Calas, C. Brouder, ^{57}Fe Mössbauer spectroscopy of tektites. *Phys. Chem. Miner.* **26**, 530–538 (1999).
54. S. Rossano, H. Behrens, M. Wilke, Advanced analyses of ^{57}Fe Mössbauer data of alumino-silicate glasses. *Phys. Chem. Miner.* **35**, 77–93 (2008).
55. A. Borisov, C. McCammon, The effect of silica on ferric/ferrous ratio in silicate melts: An experimental study using Mössbauer spectroscopy. *Am. Mineral.* **95**, 545–555 (2010).
56. H. L. Zhang, P. A. Solheid, R. A. Lange, A. Von Der Handt, M. M. Hirschmann, Accurate determination of $Fe^{3+}/\Sigma Fe$ of andesitic glass by Mössbauer spectroscopy. *Am. Mineral.* **100**, 1967–1977 (2015).
57. H. L. Zhang, M. M. Hirschmann, E. Cottrell, M. Newville, A. Lanzirotti, Structural environment of iron and accurate determination of $Fe^{3+}/\Sigma Fe$ ratios in andesitic glasses by XANES and Mössbauer spectroscopy. *Chem. Geol.* **428**, 48–58 (2016).
58. K. Lagarec, D. G. Rancourt, Extended Voigt-based analytic lineshape method for determining *N*-dimensional correlated hyperfine parameter distributions in Mössbauer spectroscopy. *Nucl. Instrum. Methods Phys. Res. B: Beam Interact. Mater. At.* **129**, 266–280 (1997).
59. R. Rüffer, A. I. Chumakov, Nuclear resonance beamline at ESRF. *Hyperfine Interact.* **97–98**, 589–604 (1996).
60. C. Prescher, C. McCammon, L. Dubrovinsky, *MossA*: A program for analyzing energy-domain Mössbauer spectra from conventional and synchrotron sources. *J. Appl. Cryst.* **45**, 329–331 (2012).
61. S. Yaroslavtsev, *SYNCmoss* software package for fitting Mössbauer spectra measured with a synchrotron Mössbauer source. *J. Synchrotron Radiat.* **30**, 596–604 (2023).
62. W. F. McDonough, S.-S. Sun, The composition of the Earth. *Chem. Geol.* **120**, 223–253 (1995).
63. A. Khan, P. A. Sossi, C. Liebske, A. Rivoldini, D. Giardini, Geophysical and cosmochemical evidence for a volatile-rich Mars. *Earth Planet. Sci. Lett.* **578**, 117330 (2022).
64. M. W. Chase, National Information Standards Organization (US), *NIST-JANAF Thermochemical Tables* (American Chemical Society, 1998), vol. 9, p. 1325.
65. M. A. Baron, G. Fiquet, G. Morard, F. Miozzi, I. Esteve, B. Doisneau, A. S. Pakhomova, Y. Ricard, F. Guyot, Melting of basaltic lithologies in the Earth's lower mantle. *Phys. Earth Planet. Inter.* **333**, 106938 (2022).
66. G. K. Pradhan, G. Fiquet, J. Siebert, A.-L. Auzende, G. Morard, D. Antonangeli, G. Garbarino, Melting of MORB at core–mantle boundary. *Earth Planet. Sci. Lett.* **431**, 247–255 (2015).
67. S. Tateno, K. Hirose, S. Sakata, K. Yonemitsu, H. Ozawa, T. Hirata, N. Hirao, Y. Ohishi, Melting phase relations and element partitioning in MORB to lowermost mantle conditions. *J. Geophys. Res. Solid Earth* **123**, 5515–5531 (2018).
68. I. Blanchard, S. Petitgirard, V. Laurenz, N. Miyajima, M. Wilke, D. C. Rubie, S. S. Lobanov, L. Hennet, W. Morgenroth, R. Tucoulou, V. Bonino, X. Zhao, I. Franchi, Chemical analysis of trace elements at the nanoscale in samples recovered from laser-heated diamond anvil cell experiments. *Phys. Chem. Miner.* **49**, 18 (2022).
69. R. A. Fischer, E. Cottrell, E. Hauri, K. K. M. Lee, M. Le Voyer, The carbon content of Earth and its core. *Proc. Natl. Acad. Sci. U.S.A.* **117**, 8743–8749 (2020).
70. M. A. Bouhifd, A. P. Jephcoat, The effect of pressure on partitioning of Ni and Co between silicate and iron-rich metal liquids: A diamond-anvil cell study. *Earth Planet. Sci. Lett.* **209**, 245–255 (2003).
71. S. K. Bajgain, A. W. Ashley, M. Mookherjee, D. B. Ghosh, B. B. Karki, S. K. Bajgain, A. W. Ashley, M. Mookherjee, D. B. Ghosh, B. B. Karki, S. K. Bajgain, A. W. Ashley, M. Mookherjee, D. B. Ghosh, B. B. Karki, S. K. Bajgain, A. W. Ashley, M. Mookherjee, D. B. Ghosh, B. B. Karki, S. K. Bajgain, A. W. Ashley, M. Mookherjee, D. B. Ghosh, B. B. Karki, S. K. Bajgain, A. W. Ashley, M. Mookherjee, D. B. Ghosh, B. B. Karki, S. K. Bajgain, A. W. Ashley, M. Mookherjee, D. B. Ghosh, B. B. Karki, S. K. Bajgain, A. W. Ashley, M. Mookherjee, D. B. Ghosh, B. B. Karki, Insights into magma ocean dynamics from the transport properties of basaltic melt. *Nat. Commun.* **13**, 7590 (2022).
72. A. J. Berry, G. A. Stewart, H. St, C. O'Neill, G. Mallmann, J. F. W. Mosselmans, A re-assessment of the oxidation state of iron in MORB glasses. *Earth Planet. Sci. Lett.* **483**, 114–123 (2018).
73. M. D. Dyar, D. G. Agresti, M. W. Schaefer, C. A. Grant, E. C. Sklute, Mössbauer spectroscopy of earth and planetary materials. *Annu. Rev. Earth Planet. Sci.* **34**, 83–125 (2006).
74. H. H. Wickman, M. P. Klein, P. A. Shirley, Paramagnetic hyperfine structure and relaxation effects in Mössbauer spectra: Fe^{57} in Ferrichrome A. *Phys. Rev.* **152**, 345–357 (1966).
75. K. D. Jayasuriya, H. St, C. O'Neill, A. J. Berry, S. J. Campbell, A Mössbauer study of the oxidation state of Fe in silicate melts. *Am. Mineral.* **89**, 1597–1609 (2004).
76. G. M. Partzsch, D. Lattard, C. McCammon, Mössbauer spectroscopic determination of Fe^{3+}/Fe^{2+} in synthetic basaltic glass: A test of empirical fO_2 equations under superliquidus and subliquidus conditions. *Contrib. Mineral. Petrol.* **147**, 565–580 (2004).
77. E. De Grave, A. Van Alboom, Evaluation of ferrous and ferric Mössbauer fractions. *Phys. Chem. Miner.* **18**, 337–342 (1991).
78. M. Roskosz, N. Dauphas, J. Hu, M. Y. Hu, D. R. Neuville, D. Brown, W. Bi, N. X. Nie, J. Zhao, E. E. Alp, Structural, redox and isotopic behaviors of iron in geological silicate glasses: A NRIXS study of Lamb-Mössbauer factors and force constants. *Geochim. Cosmochim. Acta* **321**, 184–205 (2022).
79. R. E. Vandenberghe, A. E. Verbeeck, ^{57}Fe Mössbauer effect study of Mn-substituted goethite and hematite. *Hyperfine Interact.* **29**, 1157–1160 (1986).
80. J. C. Waerenborgh, J. Figueiras, A. Mateus, M. Gonçalves, ^{57}Fe Mössbauer spectroscopy study of the correlation between the Fe^{3+} content and the magnetic properties of natural Cr-spinels. *Eur. J. Mineral.* **14**, 437–446 (2002).
81. E. De Grave, A. Van Alboom, S. G. Eeckhout, Electronic and magnetic properties of a natural aegirine as observed from its Mössbauer spectra. *Phys. Chem. Miner.* **25**, 378–388 (1998).
82. S. G. Eeckhout, E. De Grave, C. A. McCammon, R. Vochten, Temperature dependence of the hyperfine parameters of synthetic $P2_1/c$ Mg-Fe clinopyroxenes along the $MgSiO_3$ -$FeSiO_3$ join. *Am. Mineral.* **85**, 943–952 (2000).
83. S. G. Eeckhout, E. De Grave, C. A. McCammon, R. Vochten, Mössbauer study of synthetic $Mg_{0.22}Fe_{0.78}SiO_3$ clinopyroxene. *Mineral. Petrol.* **73**, 235–245 (2001).
84. S. G. Eeckhout, E. De Grave, ^{57}Fe Mössbauer-effect studies of Ca-rich, Fe-bearing clinopyroxenes: Part I. Paramagnetic spectra of magnesian hedenbergite. *Am. Mineral.* **88**, 1129–1137 (2003).
85. E. De Grave, S. G. Eeckhout, ^{57}Fe Mössbauer-effect studies of Ca-rich, Fe-bearing clinopyroxenes: Part III. Diopside. *Am. Mineral.* **88**, 1145–1152 (2003).
86. A. B. Woodland, C. R. Ross II, A crystallographic and Mössbauer spectroscopy study of $Fe_3^{2+}Al_2Si_3O_{12}$-$Fe_3^{2+}Fe_2^{3+}Si_3O_{12}$, (almandine-"skiagite") and $Ca^{3+}Si_3O_{12}$-$Fe_3^{2+}Fe_2^{3+}Si_3O_{12}$(andradite-"skiagite") garnet solid solutions. *Phys Chem Miner.* **21**, 117–132 (1994).
87. M. D. Dyar, E. A. Breves, E. Emerson, S. W. Bell, M. Nelms, M. V. Ozanne, S. E. Peel, M. L. Carmosino, J. M. Tucker, M. E. Gunter, J. S. Delaney, A. Lanzirotti, A. B. Woodland, Accurate determination of ferric iron in garnets by bulk Mössbauer spectroscopy and synchrotron micro-XANES. *Am. Mineral.* **97**, 1726–1740 (2012).
88. T. Komabayashi, Thermodynamics of melting relations in the system Fe-FeO at high pressure: Implications for oxygen in the Earth's core. *J. Geophys. Res. Solid Earth* **119**, 4164–4177 (2014).
89. R. O. Sack, I. S. E. Carmichael, M. Rivers, M. S. Ghiorso, Ferric-ferrous equilibria in natural silicate liquids at 1 bar. *Contrib. Mineral. Petrol.* **75**, 369–376 (1981).
90. V. C. Kress, I. S. E. Carmichael, The compressibility of silicate liquids containing Fe_2O_3 and the effect of composition, temperature, oxygen fugacity and pressure on their redox states. *Contrib. Mineral. Petrol.* **108**, 82–92 (1991).
91. A. Borisov, H. Behrens, F. Holtz, Ferric/ferrous ratio in silicate melts: A new model for 1 atm data with special emphasis on the effects of melt composition. *Contrib. Mineral. Petrol.* **173**, 98 (2018).
92. B. Dingwell, M. Brearley, J. Dickinson, Melt densities in the Na_2O-FeO-Fe_2O_3-SiO_2 system and the partial molar volume of tetrahedrally-coordinated ferric iron in silicate inelts. *Geochim. Cosmochim. Acta* **52**, 2467–2475 (1988).
93. R. A. Lange, I. S. E. Carmichael, Densities of Na_2O-K_2O-CaO-MgO-FeO-Fe_2O_3-Al_2O_3-TiO_2-SiO_2 liquids: New measurements and derived partial molar properties. *Geochim. Cosmochim. Acta* **51**, 2931–2946 (1987).
94. R. A. Lange, A. Navrotsky, Heat-capacities of Fe_2O_3-bearing silicate liquids. *Contrib. Mineral. Petrol.* **110**, 311–320 (1992).
95. H. E. Schlichting, S. Mukhopadhyay, Atmosphere impact losses. *Space Sci. Rev.* **214**, 34 (2018).
96. J. Blundy, E. Melekhova, L. Ziberna, M. C. S. Humphreys, V. Cerantola, R. A. Brooker, C. A. McCammon, M. Pichavant, P. Ulmer, Effect of redox on Fe–Mg–Mn exchange between olivine and melt and an oxybarometer for basalts. *Contrib. Mineral. Petrol.* **175**, 103 (2020).
97. C. Prescher, F. Langenhorst, L. S. Dubrovinsky, V. B. Prakapenka, N. Miyajima, The effect of Fe spin crossovers on its partitioning behavior and oxidation state in a pyrolitic Earth's lower mantle system. *Earth Planet. Sci. Lett.* **399**, 86–91 (2014).
98. F. Maeda, S. Kamada, E. Ohtani, N. Hirao, T. Mitsui, R. Masuda, M. Miyahara, C. McCammon, Spin state and electronic environment of iron in basaltic glass in the lower mantle. *Am. Mineral.* **102**, 2106–2112 (2017).
99. S. M. Dorfman, S. E. Dutton, V. Potapkin, A. I. Chumakov, J.-P. Rueff, P. Chow, Y. Xiao, R. J. Cava, T. S. Duffy, C. A. McCammon, P. Gillet, Electronic transitions of iron in almandine-composition glass to 91 GPa. *Am. Mineral.* **101**, 1659–1667 (2016).
100. S. Anzellini, V. Monteseguro, E. Bandiello, A. Dewaele, L. Burakovsky, D. Errandonea, In situ characterization of the high pressure—High temperature melting curve of platinum. *Sci. Rep.* **9**, 13034 (2019).

101. S. Anzellini, A. Dewaele, M. Mezouar, P. Loubeyre, G. Morard, Melting of iron at Earth's inner core boundary based on fast x-ray diffraction. *Science* **340**, 464–466 (2013).

Acknowledgments: We thank J. Drewitt for assistance with levitation heating; B. Buse, S. Kearns, and W.-C. Li for assistance with EPMA; and S. Aithala for helping E-SMS collection. We thank T. Gooding for the recovered sample preparation method. Discussions with C.A. McCammon are greatly appreciated. **Funding:** H.L.Z. has been supported by the National Natural Science Foundation of China (grant nos. 42150102 and 41873067). M.M.H. has been supported by the U.S. National Science Foundation (grant nos. EAR2016215 and EAR2317026). O.T.L. was supported by the Royal Society in the form of a University Research Fellowship (UF150057). E.C. was supported by a Smithsonian NMNH Core Grant. H.L.Z, O.T.L., and M.J.W were also supported by the NERC thematic action programme "The Volatile Legacy of the Deep Earth" (NE/M000419/1). We acknowledge the European Synchrotron Radiation Facility for provision of beamtime at ID18 Nuclear Resonance Beamline (ES-1330). **Author contributions:** Conceptualization: M.M.H. and M.J.W. Sample synthesis: H.L.Z., O.T.L., and M.J.W. Data collection: H.L.Z., M.M.H., A.R., S.Y., A.I.C., and E.C. Data reduction: H.L.Z., A.R., and S.Y. Thermodynamic model: H.L.Z. and M.M.H. Visualization: H.L.Z. and M.M.H. Funding acquisition: H.L.Z, M.M.H, O.T.L., M.J.W., and E.C. Writing—original draft: H.L.Z. and M.M.H. Writing—review and editing: H.L.Z., M.M.H., O.T.L., M.J.W., A.R., S.Y., A.I.C., and E.C. **Competing interests:** The authors declare that they have no competing interests. **Data and materials availability:** All data needed to evaluate the conclusions in the paper are present in the paper and/or the Supplementary Materials.

Submitted 11 March 2024
Accepted 12 September 2024
Published 16 October 2024
10.1126/sciadv.adp1752